The numerical simulation of clouds, rain, and airflow over the Voges and Black Forest Mountains: a Meso-beta model with parameterized microphysics

Everett C. Nickerson, Evelyne Richard, R. Rosset, David R. Smith

The Numerical Simulation of Clouds, Rain, and Airflow over the Vosges and Black Forest Mountains: A Meso-β Model with Parameterized Microphysics

EVERETT C. NICKERSON

National Oceanic and Atmospheric Administration, Air Resources Laboratory, GMCC, Boulder, CO 80303

EVELYNE RICHARD AND ROBERT ROSSET

Laboratoire Associé de Météorologie Physique, Clermont-Ferrand, 63170, Aubière, France

DAVID R. SMITH*

National Oceanic and Atmospheric Administration, Air Resources Laboratory, GMCC, Barrow, AK 99723

(Manuscript received 19 December 1983, in final form 9 September 1985)

ABSTRACT

A three-dimensional meso-β model with parameterized microphysics is presented. The model is capable of simulating orographically forced clouds, rain, and airflow. Tests using a two-dimensional version confirm the ability of the model to replicate the linear and nonlinear mountain wave simulations of previous authors. The model is applied to the Rhine valley and surrounding mountainous areas, the Vosges in France and the Black Forest in Germany. Model-predicted rainfall over the mountainous areas is in good agreement with observations in both magnitude and location; however, an absence of model-predicted cloud cover over the Rhine valley suggests the need for an improved mesoscale initialization procedure.

1. Introduction

Local convergence and vertical motion fields induced within air flowing over irregular terrain can significantly influence the location, the intensity, and even the microphysics of precipitation reaching the ground. Studies of precipitation patterns over the British Isles (Browning et al., 1974), New Zealand (Salinger, 1980), and Hawaii (Lavoie et al., 1967) have documented the strong effects of orography on the initiation, enhancement, and/or suppression of precipitation. Although it is not surprising to discover such effects in the presence of large mountain barriers, Bergeron (1965) has shown that even relatively small orographic features less than 100 m high can, under the proper conditions, profoundly affect local precipitation patterns (Weickmann, 1979). Numerical simulations of orographically induced precipitation present us with an opportunity to evaluate the performance of mesoscale models under much simpler conditions than would normally be found in synoptically induced mesoscale systems (Pielke, 1981).

Numerical models have demonstrated an ability to provide realistic simulations of mesoscale weather systems (Anthes and Warner, 1978; Chang et al., 1981). However, an accurate prediction of the amount and to a lesser extent the location of precipitation has remained an elusive goal (Warner et al., 1978; Anthes and Haagenson, 1983). Among the reasons for the discrepancies between observed and forecast precipitation rates are the horizontal resolution of the model (especially in regions of complex terrain), and the procedures used to parameterize the precipitation processes. Another important consideration is the specification of the initial moisture fields and the associated vertical motion necessary to maintain saturation (Tarbell et al., 1981).

In order to simulate both the temporal and spatial variability of precipitation reaching the ground, it may be necessary to resolve in detail the complete microphysical sequence of events, and to significantly reduce the horizontal grid increment. In the sections which follow we first present a mesoscale model with a microphysical parameterization based upon an assumed lognormal raindrop distribution. The rainwater mixing ratio and raindrop concentration are calculated from separate predictive equations. This approach is considerably less complex than that of Young (1974), or Takahashi (1979), but allows for an extra degree of freedom not present in the Kessler parameterization used for example by Clark (1979).

Simulations of a two-dimensional nature are then discussed. These were carried out to test the ability of the model to correctly replicate the linear and nonlinear numerical mountain wave solutions obtained by pre-

* Presently privately employed in Pt. Barrow, AK.

vious authors (Klemp and Lilly, 1978; Mahrer and Pielke, 1978). We then test the performance of the three-dimensional model by carrying out a simulation of a rainfall event over the mountains surrounding the Rhine valley along the French–German border. This region will be the site of future field programs involving wet and dry deposition in the Vosges and Black Forest mountains, and it is anticipated that the model will be used in the design and interpretation of those studies.

2. The model

The three-dimensional meso-β model of Nickerson (1979) is extended here to include warm rain microphysical processes. The equations are written in a system of local coordinates (x, y, ν) where the vertical coordinate ν is related to the usual sigma pressure coordinate by $\sigma = (4\nu - \nu^4)/3$. Here $\sigma = (P - P_T)/\Pi$, where $\Pi = P_S - P_T$ represents the difference in pressure between the lower and upper boundaries. The vertical coordinate represents a simple ad hoc transformation in which the new vertical coordinate ranges from unity to zero as in the conventional sigma system. The vertical coordinate also satisfies the condition that $d\sigma/d\nu$ must be finite over the entire domain and must be equal to zero at the lower boundary to assure second-order accuracy in the discretization scheme (De Rivas, 1972). The terrain-following coordinate ν was incorporated into the model and permits the use of a constant vertical grid increment $\Delta\nu$ while providing for an improved vertical resolution of meteorological parameters in the planetary boundary layer. (See Table 1 for a comparison of the σ and ν coordinate systems.)

a. Dynamical equations

The prognostic equations for the variables $U = \Pi u$ and $V = \Pi v$ are written in the ν coordinate system as

$$\frac{\partial U}{\partial t} = -\frac{\partial(Uu)}{\partial x} - \frac{\partial(Uv)}{\partial y} - \frac{1}{\sigma'}\frac{\partial(\sigma' U\dot{\nu})}{\partial \nu} + fV + \left(\Phi - \frac{R_v T^* \sigma \Pi}{P}\right)\frac{\partial \Pi}{\partial x} - \frac{\partial(\Pi\Phi)}{\partial x} + F_u, \quad (1)$$

$$\frac{\partial V}{\partial t} = -\frac{\partial(Vu)}{\partial x} - \frac{\partial(Vv)}{\partial y} - \frac{1}{\sigma'}\frac{\partial(\sigma' V\dot{\nu})}{\partial \nu} - fU + \left(\Phi - \frac{R_v T^* \sigma \Pi}{P}\right)\frac{\partial \Pi}{\partial y} - \frac{\partial(\Pi\Phi)}{\partial y} + F_v, \quad (2)$$

where u and v are the usual horizontal wind components, Φ is the geopotential, and F_u and F_v are the friction terms. Each friction term consists of a vertical eddy diffusion term representing the turbulent transport of a variable within the planetary layer (Nickerson, 1979), and a horizontal diffusion term of the form

$$\Pi K_H\left(\frac{\partial^2}{\partial x^2} + \frac{\partial^2}{\partial y^2}\right)$$

operating on a ν surface. Other symbols are defined in appendix A.

The vertical velocity $\dot{\nu}$ is given by

$$\dot{\nu} = -\frac{1}{\Pi\sigma'}\int_0^{\nu} \sigma'\left(\frac{\partial \Pi}{\partial t} + \frac{\partial U}{\partial x} + \frac{\partial V}{\partial y}\right)d\nu^*. \quad (3)$$

The temporal evolution of the surface pressure is obtained from the vertical integration of the equation of continuity:

$$\frac{\partial \Pi}{\partial t} = -\int_0^1 \left(\frac{\partial U}{\partial x} + \frac{\partial V}{\partial y}\right)\sigma' d\nu. \quad (4)$$

The geopotential Φ is calculated as follows:

$$\frac{\partial \Phi}{\partial \tilde{P}} = -C_p\theta(1 + 0.61q_v). \quad (5)$$

b. Thermodynamical equations

The predicted thermodynamic variables are an entropy variable $S = \Pi H$, and a moisture variable $W = \Pi(q_v + q_{cw})$, where q_v and q_{cw} are mixing ratios of water vapor and cloud water, respectively. Apart from a small correction factor (of order 10^{-3}) which is proportional to the mixing ratio of liquid water present in the model, the entropy variable is the same as that given by Dufour and Van Mieghem (1975), which is conserved during both dry and wet reversible adiabatic transformations:

$$H = \ln\left(\frac{T}{\tilde{P}}\right) + \frac{L_v q_v}{C_p T}. \quad (6)$$

However, in contrast to the earlier version of the model in which the condensation products remained in the air (Nickerson, 1979), the present version consists of an open system in which precipitation particles carry

TABLE 1. Comparison of the σ and ν coordinate systems.

ν	σ
0.0000	0.0000
0.0333	0.0444
0.1000	0.1333
0.1667	0.2220
0.2333	0.3101
0.3000	0.3973
0.3667	0.4829
0.4333	0.5660
0.5000	0.6458
0.5667	0.7212
0.6333	0.7908
0.7000	0.8533
0.7667	0.9071
0.8333	0.9504
0.9000	0.9813
0.9667	0.9978
1.0000	1.0000

away some of the heat gained during the precipitation process. Fortunately, such effects are quite small in this pseudoadiabatic, pseudoreversible system (Hess, 1959), since the predicted values of rainwater mixing ratio are usually less than 0.5 g kg^{-1}.

The corresponding prognostic equations are given by

$$\frac{\partial S}{\partial t} = -\frac{\partial (Su)}{\partial x} - \frac{\partial (Sv)}{\partial y} - \frac{1}{\sigma'}\frac{\partial (\sigma' S\dot{\nu})}{\partial \nu} + F_S + \text{PROS}, \tag{7}$$

$$\frac{\partial W}{\partial t} = -\frac{\partial (Wu)}{\partial x} - \frac{\partial (Wv)}{\partial y} - \frac{1}{\sigma'}\frac{\partial (\sigma' W\dot{\nu})}{\partial \nu} + F_W + \text{PROQW}. \tag{8}$$

Temperature and cloud water mixing ratio are not explicitly predicted by the model, but are diagnosed from the predicted values of S and W (Nickerson, 1979). In the event of supersaturation with respect to liquid water, excess vapor is converted into cloud water. The term PROQW represents the transformation between cloud water and rainwater, and is explained in section 2c. The term PROS, which includes radiative processes and other diabatic effects, is zero in this warm-rain model. Radiative cooling in very shallow layers at the bases and tops of clouds may exceed 6°C d^{-1}, with some slight warming possible under the clouds on the order of 1°C d^{-1} (Stearns, 1983). But Stearns also showed that the calculated radiative heating and cooling rates are very sensitive to the choice of vertical grid resolution. For simulations on the order of 6 to 8 hours, the most important neglected radiative effects are probably not the calculated in situ heating or cooling rates, but rather the evolving surface temperature field, and the possibility that clouds in the model will modify the amount of radiation reaching the ground.

c. *Microphysical equations*

Liquid water in the model is partitioned into two categories: rainwater, which falls through the air; and cloud water, which wafts around with the air. Rainwater is assumed to be distributed lognormally with diameter; that is,

$$dN_r = \frac{N_r}{(2\pi)^{1/2}\sigma_0 D}\exp\left[-\frac{1}{2\sigma_0{}^2}\ln^2\left(\frac{D}{D_0}\right)\right]dD \tag{9}$$

is the number of raindrops in the size range D to $D + dD$, and N_r is the total number of raindrops. Here σ_0 and D_0 are distribution parameters. Markowitz (1976) found that the lognormal distribution adequately described the average spectra for a number of rainfalls of several intensities.

If the diameter D_0 is large enough so that cloud-size droplets contribute very little to the total number concentration, the integration of (9) over the entire spectrum of drops of mass $\pi\rho_l D^3/6$ yields the following expression for q_r, the rainwater mixing ratio:

$$q_r = \frac{N_r}{\rho}\left(\frac{\pi}{6}D_0{}^3\rho_l\right)\exp\left(\frac{9}{2}\sigma_0{}^2\right), \tag{10}$$

where ρ and ρ_l represent the density of air and liquid water respectively. It will also be convenient to define a mean drop diameter $\overline{D_r}$, which is the diameter the raindrops would have if they were all the same size. $\overline{D_r}$ is related to the lognormal distribution parameters by

$$\overline{D_r} = D_0\exp\left(\frac{3}{2}\sigma_0{}^2\right). \tag{11}$$

Since there are two independent distribution parameters σ_0 and D_0, only one of which can be diagnosed given q_r and N_r, we close the microphysical system of equations by assuming a constant value for σ_0 and computing $\overline{D_r}$. For the model runs reported here, $\sigma_0 = 0.5$.

We have made extensive use of the work of Berry and Reinhardt (1973) in developing parameterizations for autoconversion, accretion, and selfcollection processes appropriate to the lognormal raindrop distribution. Because the present cloud water formulation does not permit supersaturation with respect to water, we assume that diffusional growth of raindrops can be neglected.

Separate prognostic equations are written for both rainwater mixing ratio and total number concentration:

$$\frac{\partial \Pi q_r}{\partial t} = -\text{A}(q_r) + \Pi\left.\frac{\partial q_r}{\partial t}\right|_{\text{auto}} + \Pi\left.\frac{\partial q_r}{\partial t}\right|_{\text{accr}} + \Pi\left.\frac{\partial q_r}{\partial t}\right|_{\text{eva}} + \Pi\left.\frac{\partial q_r}{\partial t}\right|_{\text{sed}} + F_{q_r}, \tag{12}$$

$$\frac{\partial \Pi N_r}{\partial t} = -\text{A}(N_r) + \Pi\left.\frac{\partial N_r}{\partial t}\right|_{\text{auto}} + \Pi\left.\frac{\partial N_r}{\partial t}\right|_{\text{self}} + \Pi\left.\frac{\partial N_r}{\partial t}\right|_{\text{sed}} + F_{N_r}, \tag{13}$$

where the operator A applied to a variable q is defined by

$$\text{A}(q) = \frac{\partial}{\partial x}(qU) + \frac{\partial}{\partial y}(qV) + \frac{\Pi}{\sigma'}\frac{\partial}{\partial \nu}(\sigma' q\dot{\nu}). \tag{14}$$

The terms for autoconversion, selfcollection, accretion, evaporation, and sedimentation are given in appendix B. Let us note, however, that selfcollection affects only the concentration of raindrops, while accretion affects only the mixing ratio. And although the accretion and autoconversion processes represent source terms in the rainwater equations, they are at the same time sink terms for cloud water and are therefore incorporated into the term PROQW for the prediction of W in (8).

d. Numerical procedure

The computational grid and discretization scheme are based on Anthes and Warner (1978), and are presented in detail in Nickerson (1979). The $2\Delta x$ smoother (Shapiro, 1970) that was previously applied to pressure-weighted wind fields has been removed and replaced by explicit horizontal diffusion on each prognostic variable. The nondimensional value of the horizontal background diffusion is 10^{-4}.

Centered differences are used to represent the time derivative, and an Asselin filter with a coefficient of 0.25 (Schlesinger et al., 1983) is applied to avoid splitting between odd and even time steps. The time step is 10 seconds.

The model domain is 250 km on a side and has a horizontal grid length of 10 km. The vertical grid consists of 15 equally spaced levels in the ν coordinate system. The first grid point is located approximately 15 m above the underlying terrain, and there are four computational levels in the lowest kilometer. The physical separation between computational levels increases with increasing altitude.

e. Initial conditions

The model is initialized with a single radiosounding. Temperature, vapor mixing ratio, and horizontal winds are initially horizontally uniform throughout the model domain and are interpolated to the ν coordinate surfaces. No attempt has been made to provide for an initial balance between the mass and momentum fields, but rather the model itself attains that balance during the course of the numerical simulation. At the beginning of the simulation, all the microphysical variables are set equal to zero.

f. Boundary conditions

The model makes use of stability-dependent surface layer formulations for the vertical fluxes of momentum and sensible heat (Nickerson and Smiley, 1975; Benoit, 1977; Nickerson, 1979). A constant flux layer exists between the lower boundary, where z_0 has a constant value of 1 cm, and the lowest grid point in the model, which occurs at a height of approximately 15 m. Although a larger value of z_0 would perhaps have been more appropriate, the predicted wind, temperature, and moisture fields are relatively insensitive to the particular value selected for z_0. The surface values of S and W change only in response to changes in surface pressure, since temperature, vapor mixing ratio, and cloud water mixing ratio at the lower boundary retain their initial values.

The planetary boundary layer is assumed to have a constant depth of 1 km in which the exchange coefficients are computed in accordance with the profile given by O'Brien (1970). The value selected for the depth of the planetary boundary layer is appropriate for steady state, neutrally stratified conditions (Sutton, 1953; Pielke, 1981), and is in agreement with the structure of the sounding used in the case study.

The vertical velocity $\dot{\nu}$ is set to zero at the upper boundary defined by $P_T = 100$ mb. To minimize reflection from the upper boundary, we use a viscous damping layer at the top of the domain, similar to that used by Klemp and Lilly (1978) to absorb vertically propagating waves. This absorbing layer takes the following form:

$$K_H = \begin{cases} K_{H_0} & \text{for } k \geq 5 \\ K_{H_0} + \hat{K}_H \left[\sin \dfrac{\Pi}{2} \left(\dfrac{\sigma_5 - \sigma_k}{\sigma_5} \right) \right]^2 & \text{for } k < 5, \end{cases}$$

where K_{H_0} is the background diffusion and $\hat{K}_H$ the maximum diffusion value of the wave-absorbing coefficient at the top level in the model. The nondimensional value used for $\hat{K}_H$ is 0.10.

The normal velocity component at the lateral boundaries is computed using Orlanski's type of boundary conditions (Orlanski, 1976). The tangential velocity and all other prognostic variables are computed according to an advective formulation at outflow boundary points and are specified at inflow boundary points.

3. Two-dimensional model verification

A two-dimensional version was developed to assess the ability of the model to replicate previous numerical simulations of airflow over an idealized mountain. The subsections that follow describe results of several experiments involving both linear and nonlinear mountain wave simulations. This two-dimensional model also provides a more economical framework for the testing of new formulations of microphysics, air chemistry, lower boundary conditions, and other physical processes.

a. Linear hydrostatic mountain waves in an isothermal atmosphere

The behavior of linear mountain waves has been studied in detail by Alaka (1960) and Smith (1979). Although the numerical model is not linear, it should produce a steady solution that closely approximates the analytical solution when the height of the mountain is very small.

In the following experiments we study the airflow over a 1 m high bell-shaped mountain of 20 km half-width. The atmosphere is initially isothermal and has a horizontal wind speed of 20 m s^{-1}. The planetary boundary layer and the surface layer have been eliminated. The background diffusion is set to zero, and $\hat{K}_H$, the maximum diffusion at the top of the absorbing layer, is set to 0.05.

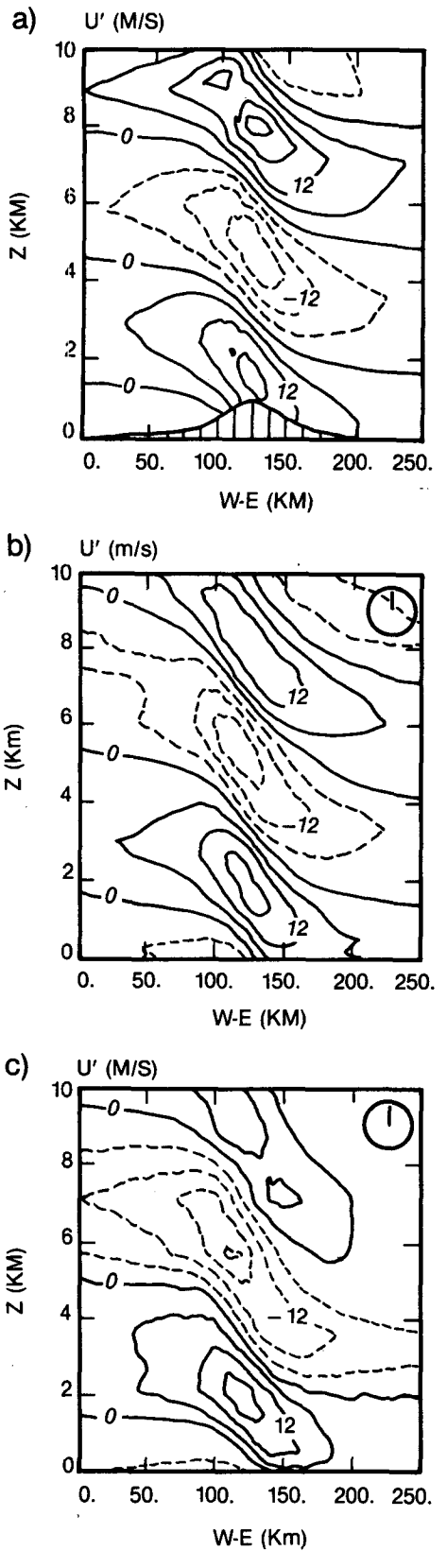

FIG. 1. Perturbation horizontal velocity from (a) the linear hydrostatic solution for a 1 km high mountain; (b) and (c) two numerical simulations with different vertical resolutions for a 1 m high mountain (amplified by a factor of 1000).

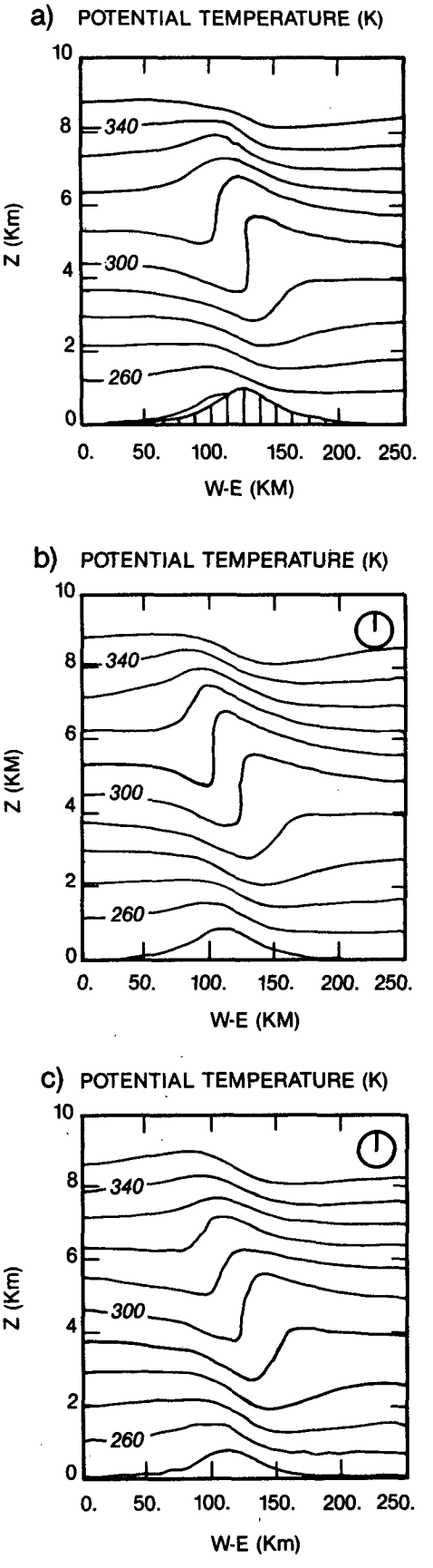

FIG. 2. As in Fig. 1, but for potential temperature.

The perturbation velocity fields in Fig. 1 show results of the analytical solution for a 1 km high mountain (case a), and two numerical solutions with different vertical resolution (cases b and c). The corresponding potential temperature fields are shown in Fig. 2. The numerical model results have been amplified by a factor of 1000 for purposes of visualization, and are shown after 12 hours of model time. This corresponds to a nondimensional time of 21.6, using the definition given in terms of the initial wind speed and the width of the mountain (Klemp and Lilly, 1978).

Simulation b was performed with 30 vertical k levels and 9 levels within the absorbing layer. The horizontal extent of the domain was 500 km, and only the central portion is shown in the figure. For simulation c, only 15 vertical levels were used, with 5 of them located within the absorbing layer. The entire horizontal domain is displayed. In both cases b and c, the absorbing layer begins at about 6 km above the ground. A comparison between cases a and b shows that there is good agreement between model results and the analytical solution below the absorbing layer. The agreement is still good in case c where the vertical resolution is much coarser and the lateral boundaries are closer to the mountain.

Figure 3 shows the vertical distribution of the numerically computed momentum flux, M, for cases b and c, normalized by the analytical linear value M_0. In the inviscid layer, the momentum flux for case b is nearly constant with height. Case c shows some difference at the interface between the absorbing layer and the inviscid layer, probably due to a lack of vertical resolution. The small oscillations more noticeable in case c than case b appear to be related to the proximity of the lateral boundaries.

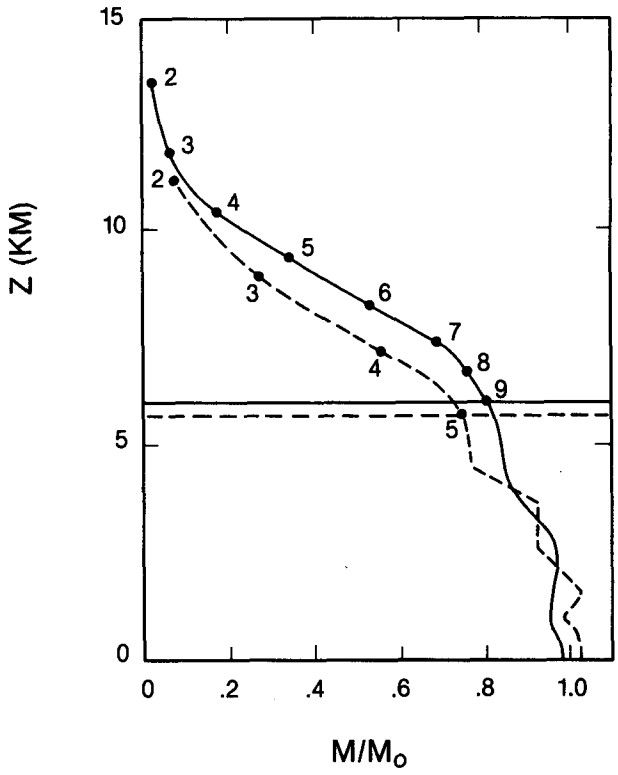

FIG. 3. Momentum flux normalized by its linear hydrostatic value for case (b) in Figs. 1 and 2 (solid line) and case (c) (dashed line). The black dots indicate for each simulation the position of the k levels within the absorbing layer.

b. *Nonlinear hydrostatic waves in a two-layer atmosphere*

To test the model for large-amplitude cases where nonlinear terms have a significant effect, we now set the height of the bell-shaped mountain to 1 km. The lowest part of the domain, below 300 mb, represents a troposphere in which the temperature decreases at a constant rate of 6°C km^{-1} from a value of 280 K at zero elevation. The region above 300 mb is isothermal and contains the wave-absorbing layer. The horizontal wind is initially 20 m s^{-1}. A constant eddy diffusion K_{H0} of 10^{-3} is applied to all prognostic variables, and the planetary boundary layer parameterization is invoked.

We performed two simulations, and the results are displayed in Figs. 4a and b. Case a is a dry case (i.e., initialized with $q_r = 0$), whereas case b is a moist case, initialized with 100% relative humidity. Experiment a is similar to Mahrer and Pielke's (1978) experiment. In spite of slight differences in initialization and parameterization of the planetary boundary layer, our results are in good agreement with the results shown in Fig. 9 of Mahrer and Pielke. A comparison of Figs. 4a and b shows, as is expected (Durran and Klemp, 1983), that the moist waves are appreciably weaker than the dry waves.

The vertical grid consisting of 15 computational levels is not really appropriate for the simulation of two-dimensional mountain waves. We could have done a better job in these experiments by increasing the vertical resolution and by using another type of vertical coordinate rather than the sigma system, but our purpose here was to run those two-dimensional experiments with a code analogous to the one used for the three-dimensional simulation. The results have demonstrated that despite the relatively coarse vertical and horizontal resolution used in the model, the solutions are quite comparable to the results obtained by other authors.

4. A case study

The Vosges–Black Forest area between France and Germany, separated by the Rhine Valley and the Alsace plain (Fig. 5), is the locale for this case study designed to test the ability of the model to simulate orographic precipitation. The two mountainous areas extend from 400 to 1500 m above sea level, and have a great influence on the local airflow and rainfall patterns.

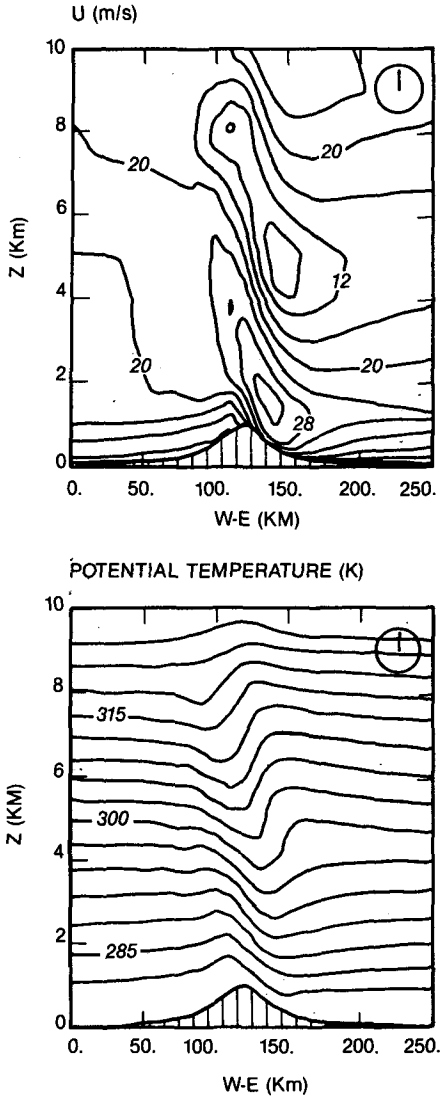

FIG. 4a. Horizontal velocity and potential temperature for the dry case with a 1-km high mountain.

During October 1976, an observational study was carried out by the Electricité de France (EDF) using a light aircraft and one special radiosonde site to provide low-level data on wind, temperature, and humidity in the southern portion of the Rhine valley. Among the rainy days of that period, 14 October was selected on the basis of the occurrence of moderate rainfall in the surrounding mountains.

a. Meteorological observations

The 1200 GMT surface pressure chart (Fig. 6) shows that the Rhine Valley area was located ahead of a cold front in a warm sector of a perturbation associated with a deep low centered over Cornwall. This resulted in a southwest wind regime over the domain.

The Nancy 1200 GMT sounding (Fig. 7), used to initialize the model, indicates that low-level air as well as the layer between 3.5 and 8 km was nearly saturated. At this station, the predominant wind direction was from the southwest. During the period 1200 to 1800 GMT, most of the stations in the domain were reporting two layers of clouds representing 6 to 8 octals of cloudiness.

Between 0900 and 1000 GMT, the EDF aircraft flew across the Rhine Valley, which is approximately 40 km wide at Colmar's latitude. The values reported for the wind direction show that the southwest wind (245° measured at 1000 m above sea level) was backing to a more southerly direction at lower altitudes (200° at 600 m and below). In general, this channeling of the synoptic flow at low levels was regularly observed all along the valley during conditions of southwesterly

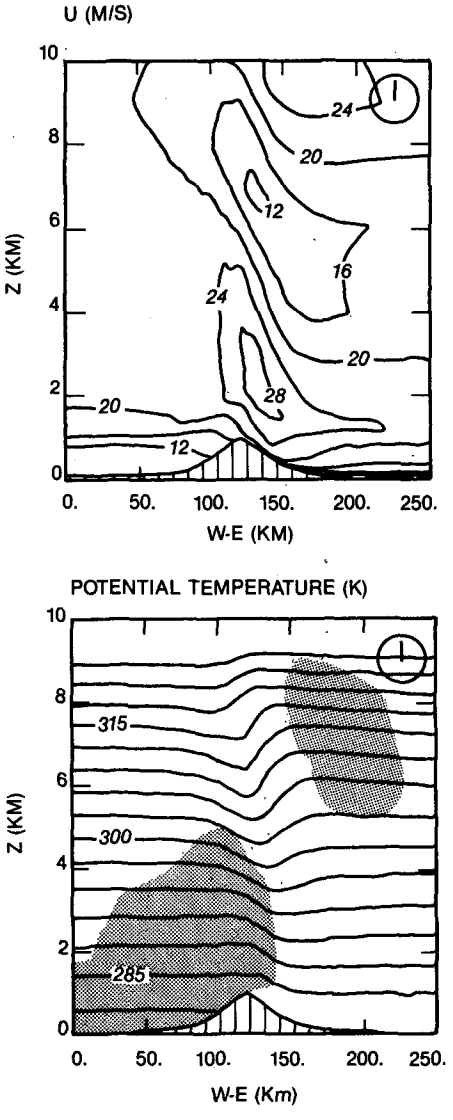

FIG. 4b. As in Fig. 4a, but for the moist case.

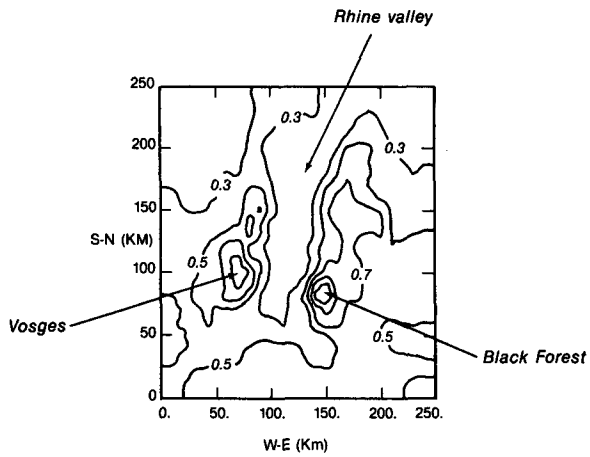

FIG. 5. Height contours of the model-testing domain.

airflow. The effect of the valley on the surface winds may be seen in Fig. 8, which shows the wind vectors corresponding to the network of surface stations.

In Fig. 9, 24-hour accumulated rainfall data from 0600 GMT 14 October to 0600 GMT 15 October are plotted using data from 361 stations in the domain. Significant precipitation occurred over the mountainous areas: 18.9 mm over the Black Forest and 11.1 mm over the Vosges.

b. Model results

At the beginning of the simulation there is an initial imbalance between the mass and momentum fields associated with the single-sounding initialization procedure. It takes approximately 2 hours for the model airflow to overcome this imbalance and adjust to the underlying terrain. Although there are still some very slight changes occurring in the wind field at the end of the 6-hour simulation, the model has apparently reached a near steady-state condition.

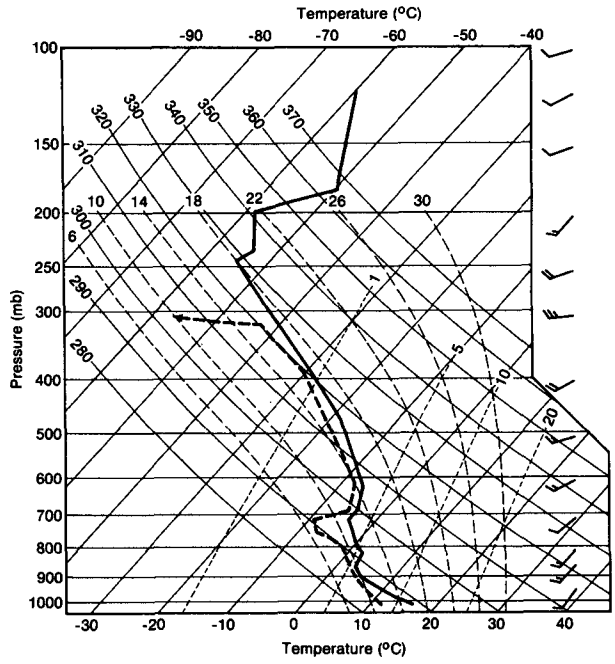

FIG. 7. Radiosonde of Nancy, France, 1200 GMT 14 October 1976. The solid line is the temperature and the dashed line the dewpoint temperature.

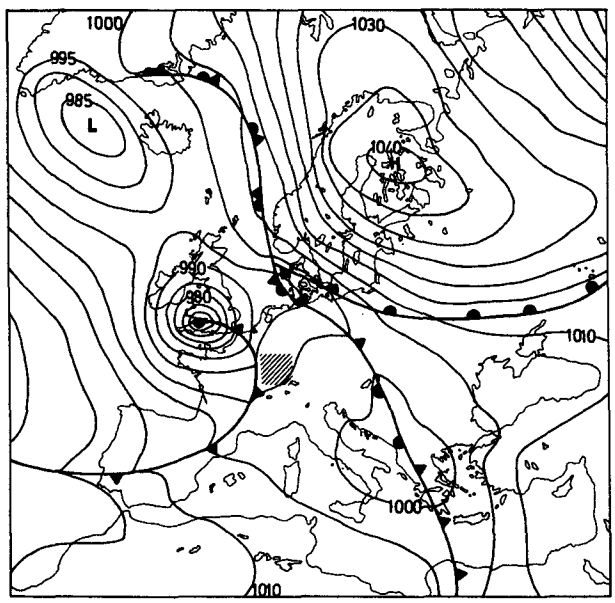

FIG. 6. Surface pressure chart (mb) for 1200 GMT 14 October 1976 from the European Meteorological Bulletin. The location of the model-testing domain is indicated by the shaded area.

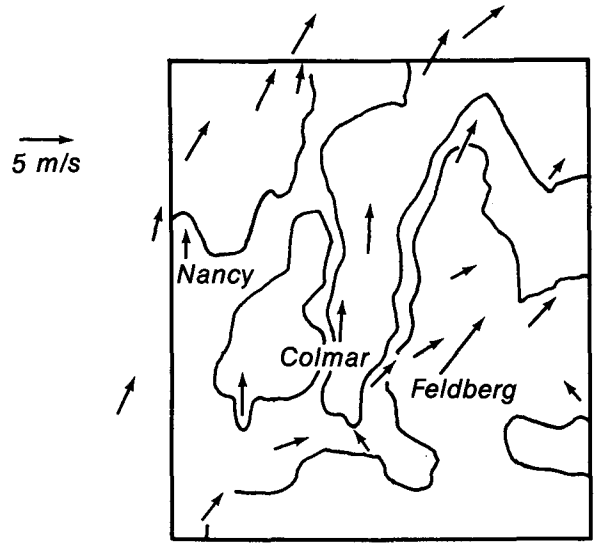

FIG. 8. Wind vectors corresponding to the network of surface stations 1200 GMT 14 October 1976. The 0.3 and 0.5 km contours of terrain are indicated.

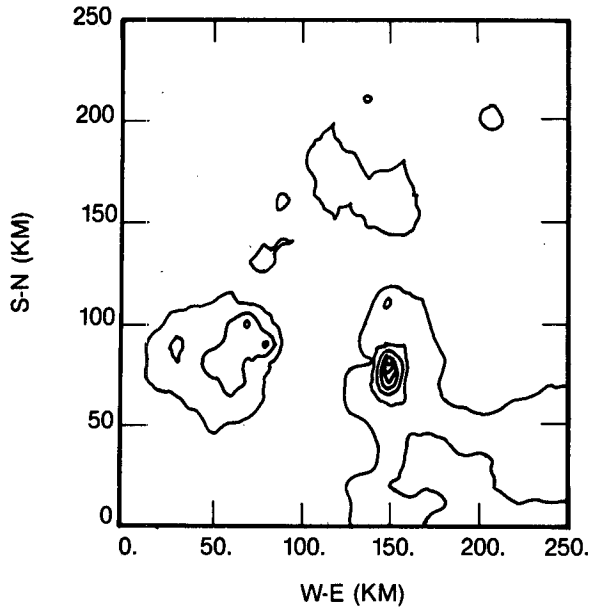

FIG. 9. Objective analysis of 24-hour accumulated rainfall data from 0600 GMT 14 October 1976 to 0600 GMT 15 October 1976. The contours are drawn every 0.2 cm starting at 0.4 cm.

Figure 10 shows the model-predicted wind field after 6 hours of simulation at a height of 600 m above sea level. Whereas the winds at each elevation were initially uniform over the entire domain, we observe in Fig. 10 the effects of the terrain in modifying the flow, especially in the Rhine Valley and in the vicinity of the mountainous areas. One notices a channeling by the valley whereby the winds have acquired a more southerly component associated with an acceleration of several meters per second. The corresponding wind field computed at the lowest level of the model is shown in Fig. 11.

As the moist air is forced up by the underlying topography, condensation occurs and clouds form above the highest mountains. Figure 12 shows contours, after 6 hours of model time, of the vertically integrated cloud water defined by

$$\overline{q_{cw}} = \frac{1}{\rho_l} \int_0^\infty \rho q_{cw} dz.$$

Figure 13 shows the spatial distribution of precipitation after 6 hours of simulation. The heaviest model-predicted rainfall (5.4 mm) occurred over the Black Forest, a little upwind of the highest Feldberg peak. Weaker precipitation occurred over the Vosges (3 mm), and a very light arc of rain fell over the northern part of the Black Forest.

We now turn our attention to two different vertical cross sections along the mean wind direction: through the Vosges massif, and through the Black Forest massif. The positions of these two cross sections are indicated respectively by lines AA′ and BB′ in Fig. 12. The cloud water mixing ratio after 1 hour of simulation (Fig. 14) shows that the model predicts two distinct cloud layers over both the Vosges and the Black Forest. Over the Black Forest (Fig. 14b), as time progresses, the lower level cloud builds up and the upper level cloud becomes weaker. Over the Vosges (Fig. 14a), it is the upper-level cloud that seems to become more active. These two

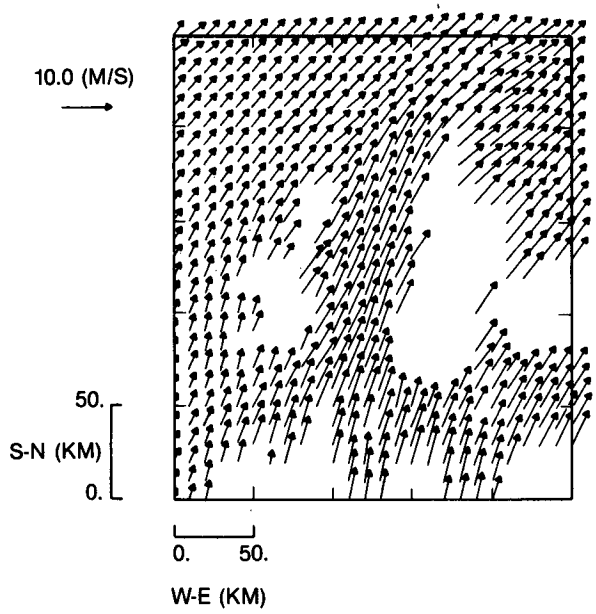

FIG. 10. Model-predicted wind field after six hours of simulation at a height of 600 m above sea level.

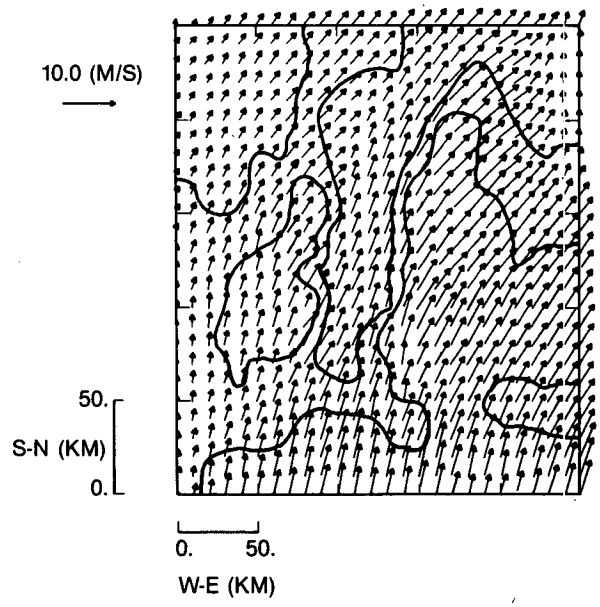

FIG. 11. Model-predicted wind field after 6 h of simulation at a height of 15 m above the ground. The 0.3 and 0.5 km contours of terrain are indicated.

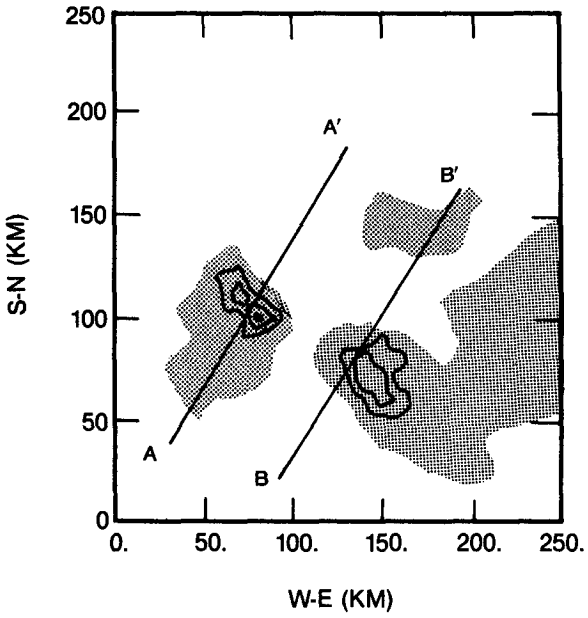

FIG. 12. Vertically integrated cloud water after 6 hours. The indicated contours are 0.03, 0.02, and 0.01 cm and the shaded area corresponds to the 0.001 cm contour. The lines AA' and BB' identify the locations of the vertical cross sections shown in Figs. 14–17.

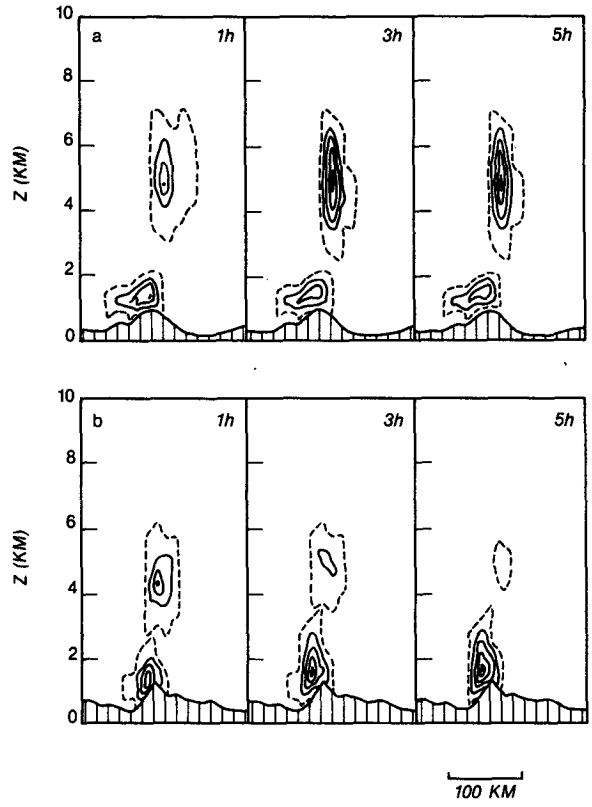

FIG. 14. Vertical cross sections of cloud water mixing ratio: (a) along AA' over the Vosges and (b) along BB' over the Black Forest; both cross sections are after 1, 3 and 5 h of simulation. The solid contours are drawn every 0.05 g kg^{-1} starting at 0.05 g kg^{-1}. The dashed line corresponds to 0.01 g kg^{-1}.

cloud layers do not have the same efficiency in producing precipitation at the ground, as can be seen in Fig. 15 where the corresponding contours for the rainwater mixing ratio have been plotted.

The lower cloud generates more rainwater above the Black Forest, and this rainwater succeeds in reaching the ground, while the upper level cloud above the Vosges produces precipitation that does not reach the ground.

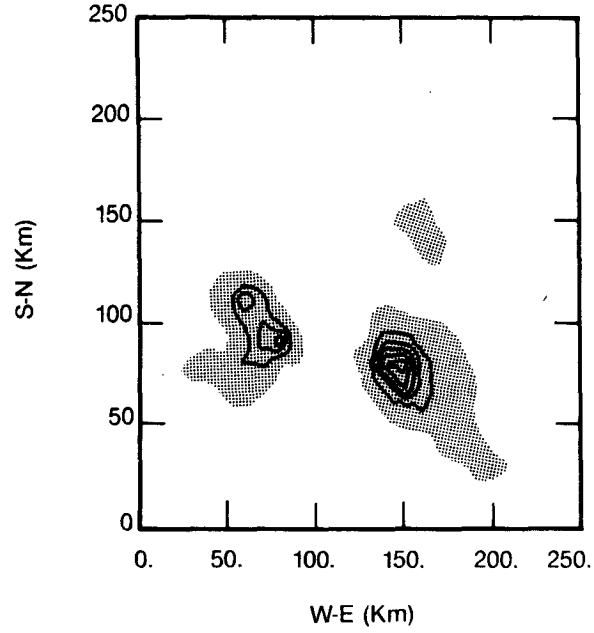

FIG. 13. Model-predicted rainfall after 6 h. The contours are indicated every 0.1 cm starting at 0.1 cm. The shaded area corresponds to 0.01 cm.

Figures 16 and 17 show for the same cross sections the contours of the raindrop concentration and the mean raindrop diameter after 5 hours of simulation. The highest concentrations are found in the lower level cloud over the two massifs (>250 drops l^{-1} for the Vosges and >350 for the Black Forest), while the largest drops are found at the bases of the upper cloud for the Black Forest, and somewhat lower for the Vosges.

5. Discussion

The model was able to reproduce the channeling of the airflow in the Rhine Valley, which was observed during the experimental period for southwest wind conditions. Even allowing for the possible unrepresentativeness of isolated surface wind observations in mountainous locations, a comparison between model predictions (Fig. 11) and observations (Fig. 8) shows reasonably good agreement over the central and northern portion of the model domain, even though the computed airflow may be adversely affected by the

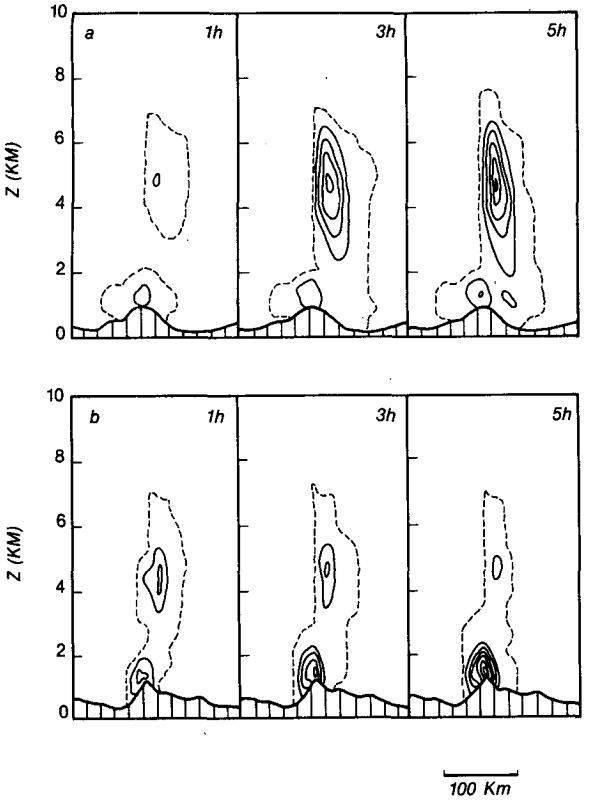

FIG. 15. As in Fig. 14, but for rainwater mixing ratio.

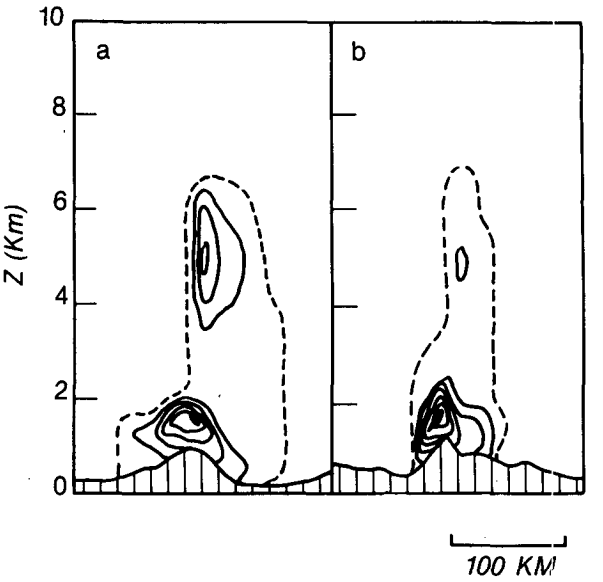

FIG. 16. Vertical cross section of the raindrop concentration: (a) along AA′ over the Vosges and (b) along BB′ over the Black Forest; both cross sections are after 5 h simulation. The solid contours are drawn every 50 drops l^{-1}, starting at 50. The dashed contour corresponds to 1 raindrop l^{-1}.

initialization procedure and an incorrect specification of the winds at the southern boundary (an inflow boundary).

During the whole course of the simulation, the cloud cover remains essentially attached to the mountains and does not spread out enough when compared with the network data. The underprediction of the zone of cloudy air over the plain is related to the present method of initialization which is based upon a single radiosonde and in which no account is taken of initial cloudiness and convergence. This procedure limits the model response to orographically forced cloud fields.

A comparison of Figs. 9 and 13 shows good agreement between the spatial distribution of observed and computed precipitation, in spite of their different integration time periods: 24 hours for the data and 6 hours for the simulation. The locations of both rainfall maxima over the Vosges and Black Forest are reproduced reasonably well by the model, as is the strong gradient observed around the Feldberg peak. In the actual field data, the precipitating zone covering the northern part of the Black Forest is more widespread over the valley. The simulation misses this feature, probably because of the initialization procedure discussed above. A quantitative comparison is not really possible because of the lack of temporal rainfall information: only three stations, all of which are located in the plain, reported rainfall over an extended period of time (from 6 to 10 hours in the 24-hour period considered). However, we notice that the maximum rainfall intensity over the Black Forest is about twice as large as that over the Vosges in both observed and computed precipitation fields.

A further discussion of the simulation results is helpful to understand why such a large difference in precipitation amounts is obtained over these two mountainous regions of almost comparable elevation.

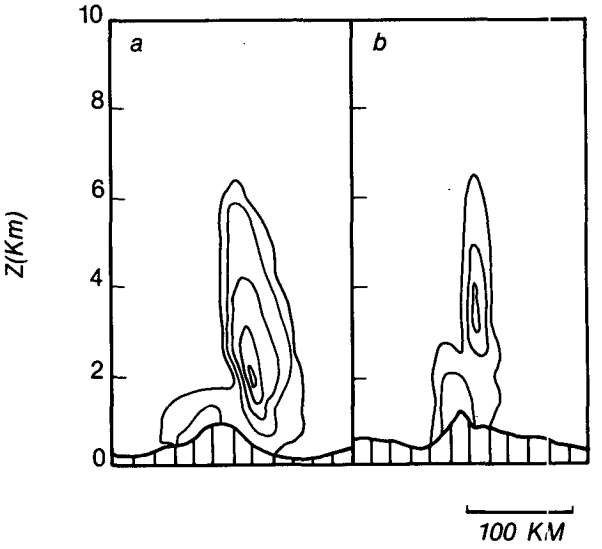

FIG. 17. As in Fig. 16, but for the mean raindrop diameter. The contours are drawn every 50 μm starting at 50 μm.

Although the elevation of their respective summits differ by only 150 m, differences in the shapes of the two massifs lead to different dynamical responses. A steeper slope and a smaller width for the Black Forest gives a higher upwind vertical velocity and a more vigorous lower cloud over this massif than over the Vosges. On the other hand, the more active cloud over the Vosges is the upper cloud, which is probably influenced by the presence of the Black Forest downwind. However, the precipitation formed in this upper cloud is not strong enough to reach the ground. Most of the raindrops are evaporated before reaching the lower cloud as can be seen in Fig. 16. The few drops that do reach the lower cloud are quite large (270 μm in Fig. 17) but not numerous enough (less than 50 l^{-1}) to enhance more active precipitation in the lower cloud.

The explicit prediction of both the mixing ratio and number concentration for the assumed lognormal droplet distribution allows the droplet spectra to evolve differently in different parts of a cloud. For example, with the same mixing ratio, one can have large numbers of small drops or small numbers of large drops within a given cloud. Such effects may not necessarily lead to a better precipitation forecast, but they are essential for other applications of the model to situations requiring knowledge of the droplet spectra.

6. Conclusions

A warm-rain microphysical parameterization based upon a lognormal drop distribution has been inserted into a three-dimensional meso-β model. A two-dimensional version has shown that the vertical resolution in the 15-layer model is adequate to damp and prevent the unwanted reflection of vertically propagating waves in the absorbing layer at the top of the model domain.

A test of the precipitation scheme has been carried out for a case of orographically forced rainfall over the Vosges and Black Forest mountains. Model-predicted rainfall is in good agreement with observations in both magnitude and location; however, the single-sounding initialization procedure does not yield realistic predictions of cloud formation over the plain. Current research efforts are attempting to alleviate this problem using spatially varying initial conditions with balanced mass and momentum fields generated within a large-scale model.

Acknowledgments. The authors gratefully acknowledge the support and encouragement of R. G. Soulage, the Air Force Geophysics Laboratory, and the Electricité de France for its support and encouragement, and Deutscher Wetterdienst and Météorologie Nationale which provided the precipitation data used in this study. The computer simulations were carried out with the support and assistance of the ECMWF, Reading, England, and also the CCVR, Palaiseau, France, Project 1920,3612.

APPENDIX A

List of Principal Symbols

C_p	specific heat at constant pressure
D	diameter of a precipitating water drop
D_0	distribution parameter for the lognormal raindrop distribution
$\overline{D_r}$	mean diameter of the raindrop distribution
E	collision efficiency
f	Coriolis parameter
F_x	friction terms relative to any prognostic variable x
g	acceleration of gravity
H	entropy
K_H	horizontal diffusion
K_{H0}	background diffusion
$\hat{K}_H$	maximum diffusion at the top of the absorbing layer
L_v	latent heat
M	momentum flux
N_r	rain drop number concentration
P	pressure
P_0	reference pressure = 1013 mb
P_S	pressure at the lower boundary
P_T	pressure at the upper boundary
$\hat{P}$	$(P/P_0)^\kappa$
q_{cw}	cloud water mixing ratio
$\bar{q}_{cw}$	vertically integrated cloud water
q_r	rainwater mixing ratio
q_v	water vapor mixing ratio
R_v	universal gas constant
S	ΠH
T	temperature
T^*	virtual temperature
u	horizontal wind speed along the x coordinate
U	Πu
v	horizontal wind speed along the y-coordinate
V	Πv
W	$\Pi(q_v + q_{cw})$
x	horizontal west–east coordinate
y	horizontal south–north coordinate
z	altitude
z_0	roughness length
Π	$(P_S - P_T)$
π	constant = 3.141592653
κ	constant = 2/7
σ	pressure coordinate defined by $\sigma = (P - P_T)/\Pi$
σ_0	distribution parameter for the lognormal raindrop distribution
ν	vertical coordinate defined by $\sigma = (4\nu - \nu^4)/3$
$\dot{\nu}$	vertical velocity
σ'	$d\sigma/d\nu$
Φ	gz
θ	potential temperature defined by $T/\hat{P}$
ρ	density of air
ρ_l	density of liquid water

APPENDIX B

Microphysical Parameterizations

B1. Autoconversion

We use the autoconversion parameterization of Berry and Reinhardt (1973). This formulation consists of a fit to the results of a bin-type model that solves the stochastic collection equation. It will be convenient to introduce to quantities x_f and x_g defined by

$$x_f = \frac{\rho q}{N}, \tag{B1.1}$$

$$x_g = \frac{1}{\rho q}\int m^2 f(m)dm, \tag{B1.2}$$

where m is the drop mass and $f(m)dm$ is the concentration of drops of mass between m and $m + dm$. (Note that the subscripts to N and q have been dropped to make the derivation more general.) Here x_f is the mass each drop would have if all drops were the same size, and corresponds to the diameter $\overline{D_r}$ in (11); x_g is the "predominant mass."

We now assume that the mass is distributed lognormally:

$$f(m) = \frac{N}{(2\pi)^{1/2}\lambda_0 m}\exp\left[-\frac{1}{2\lambda_0^2}\ln^2\left(\frac{m}{m_0}\right)\right]. \tag{B1.3}$$

Upon inserting (B1.3) into (B1.2) and expressing the drop mass in terms of diameter, with $\lambda_0 = 3\sigma_0$ and $m_0 = \pi D_0^3/6$, we obtain

$$x_g = x_f \exp(9\sigma_0^2). \tag{B1.4}$$

Berry and Reinhardt also define a variance parameter $\mathrm{var}x = (x_g/x_f) - 1$, which in terms of the lognormal distribution yields

$$\mathrm{var}x = \exp(9\sigma_0^2) - 1. \tag{B1.5}$$

This defines the relation between Berry's (1967) variance parameter that appears in the autoconversion formula and the distribution parameter σ_0. Since we assume σ_0 is constant, var$x$ is constant and

$$\sigma_0 = \frac{1}{3}[\ln(\mathrm{var}x + 1)]^{1/2}. \tag{B1.6}$$

Berry and Reinhardt derived an expression for the average growth rate of the autoconversion of cloud water to rainwater by calculating for a variety of initial conditions the time for the rainwater spectrum to reach a size corresponding to a drop radius of 50 μm. Neglecting local changes in air density, we find the rate of increase of rainwater mixing ratio expressed in mks units is

$$\left.\frac{\partial q_r}{\partial t}\right|_{\text{auto}} = 0.067\rho q_{cw}^2\left[10^{16}\left(\frac{\rho q_{cw}}{N_{cw}}\right)^{4/3}(\mathrm{var}x)^{1/2} - 2.7\right] \times \{10^4[\rho q_{cw}(\mathrm{var}x)^{1/2}/N_{cw}]^{1/3} - 1.2\}. \tag{B1.7}$$

If we now assume that σ_0 and $N_{cw} = N_{cw}/\rho q_{cw}$ are constant,

$$\left.\frac{\partial q_r}{\partial t}\right|_{\text{auto}} = \alpha\rho q_{cw}^2, \tag{B1.8}$$

where

$$\alpha = 0.067\{10^{16}\overline{N_{cw}}^{-4/3}(\mathrm{var}x)^{1/2} - 2.7\} \times \{10^4[\overline{N_{cw}}^{-1}(\mathrm{var}x)^{1/2}]^{1/3} - 1.2\}.$$

From Berry and Reinhardt, the corresponding expression for the number concentration of raindrops in mks units is

$$\left.\frac{\partial N_r}{\partial t}\right|_{\text{auto}} = 3.5 \times 10^9\rho\left.\frac{\partial q_r}{\partial t}\right|_{\text{auto}}. \tag{B1.9}$$

The quantities $\overline{N_{cw}}$ and var$x$ that appear in the coefficient α are related to the size distribution of the cloud water. Since the present formulation of the model does not include an explicit formulation for the cloud spectra, it is not possible to calculate $\overline{N_{cw}}$ and var$x$ directly. To evaluate the coefficient α, we assume that the cloud droplets are also partitioned according to a lognormal distribution for which the distribution parameters σ_0 and D_0 remain constant. This is equivalent to supposing that the mean mass of the cloud droplets remains constant. That is,

$$x_{fcw} = \frac{\rho q_{cw}}{N_{cw}}$$

is constant.

In spite of the restrictions imposed, the hypothesis is compatible with the results of Berry and Reinhardt, who found in the course of their numerical simulations that x_{fcw} tends to remain constant during the formation of hydrometeors by the stochastic coalescence of cloud drops. We have chosen $D_0 = 32.5$ μm and $\sigma_0 = 0.2203$, which then leads to a value of $\alpha = 4$.

B2. Accretion

Accretion is the process whereby cloud droplets are collected by raindrops. Differences in the terminal velocity between collector droplets and the smaller collected drops permit the treatment of accretion as a continuous process.

We consider a large collector drop of diameter D_r and terminal velocity $v(D_r)$ and let $n'(D_{cw})dD_{cw}$ denote the number of small droplets of diameter D_{cw} per unit volume of cloud. During the interval of time dt, the large drop during its fall could theoretically collect

$$\frac{\pi}{4}D_r^2[v(D_r) - v(D_{cw})]n'(D_{cw})dD_{cw}dt \tag{B2.1}$$

small droplets of diameter D_{cw} whose terminal velocity is $v(D_{cw})$. The theoretical upper limit for the capture process given by (B2.1) must be modified by the inclusion of the coalescence efficiency, $E(D_r, D_{cw})$, and the collision efficiency,

$$\gamma_c^2(D_r, D_{cw}) = \frac{\pi b^2/4}{\pi D_r^2/4}, \quad \text{(B2.2)}$$

where b is the diameter of the circle in which the small droplet must lie in order for collision to occur. Equation (B2.1) then becomes

$$\frac{\pi}{4} D_r^2[v(D_r) - v(D_{cw})]n'(D_{cw})\gamma_c^2(D_r, D_{cw})E(D_r, D_{cw}) \times dD_{cw}dt = K(D_r, D_{cw})n'(D_{cw})dD_{cw}dt. \quad \text{(B2.3)}$$

The mass gained by the collector drop is

$$K(D_r, D_{cw})m(D_{cw})n'(D_{cw})dD_{cw}dt,$$

where $m(D_{cw})$ is the mass of a cloud droplet of diameter D_{cw}.

If there are $n(D_r)dD_r$ collector drops of diameter D_r, the rate of increase of mass is given by

$$K(D_r, D_{cw})n(D_r)n'(D_{cw})m(D_{cw})dD_r dD_{cw}.$$

Upon integrating over both cloud water and rainwater spectra, we obtain the increase of rainwater content due to accretion. If, as before, the local change in air density is neglected, we obtain

$$\left.\frac{\partial q_r}{\partial t}\right|_{\text{accr}} = \frac{1}{\rho}\int_0^\infty n(D_r) \times \left[\int_0^\infty K(D_r, D_{cw})n'(D_{cw})m(D_{cw})dD_{cw}\right]dD_r. \quad \text{(B2.4)}$$

By the integral mean value theorem, we know that there exists a diameter D_{cw}^* such that

$$\left.\frac{\partial q_r}{\partial t}\right|_{\text{accr}} = \frac{1}{\rho}\int_0^\infty n(D_r)K(D_r, D_{cw}^*) \times \left[\int_0^\infty n'(D_{cw})m(D_{cw})dD_{cw}\right]dD_r = q_{cw}\int_0^\infty n(D_r)b_a(D_r, D_{cw}^*)m(D_r)dD_r, \quad \text{(B2.5)}$$

where

$$b_a(D_r, D_{cw}^*) = \frac{K(D_r, D_{cw}^*)}{m(D_r)}.$$

Upon applying the integral mean value theorem a second time, (B2.5) becomes

$$\left.\frac{\partial q_r}{\partial t}\right|_{\text{accr}} = \rho q_r q_{cw} b_a(D_r^*, D_{cw}^*), \quad \text{(B2.6)}$$

where

$$b_a(D_r^*, D_{cw}^*) = \left(\frac{6}{\pi\rho D_r^{*3}}\right) \times \left[\frac{\pi}{4} D_r^2\gamma_c^2(D_r^*, D_{cw}^*)E(D_r^*, D_{cw}^*)\right][v(D_r^*) - v(D_{cw}^*)].$$

In the parameterization of Berry, one assumes that $D_r^* = D_{gr}$ and $D_{cw}^* = \overline{D_{cw}}$, where D_{gr} is the diameter corresponding to the predominant mass x_{gr} relative to the rainwater spectrum, $\overline{D_{cw}}$ the mean diameter of the cloud droplets. We therefore let

$$D_r^* = D_{gr} = \left(\frac{6\rho q_r}{\pi\rho_l N_r}\right)^{1/3} \exp(3\sigma_0^2),$$

$$D_{cw}^* = \overline{D_{cw}} = \left(\frac{6\rho q_{cw}}{\pi\rho_l N_{cw}}\right)^{1/3}.$$

Upon assuming that the coalescence efficiency is one, (B2.6) then becomes

$$\left.\frac{\partial q_r}{\partial t}\right|_{\text{accr}} = \frac{3\rho q_r q_{cw}}{2\rho_l D_{gr}}\gamma_c^2(D_{gr}, \overline{D_{cw}})[v(D_{gr}) - v(\overline{D_{cw}})]. \quad \text{(B2.7)}$$

For evaluation of the collision efficiency, we follow Berry (1967) and adopt the following approximation to the data of Shafrir and Neiburger (1963):

$$\gamma_c(r_l, p) = 1 + p + \frac{d}{p^f} + \frac{e}{(1-p)^g}, \quad \text{(B2.8)}$$

where $p = r_s/r_l$ is the ratio of the radius of the small drop to the radius of the collector drop, and where

$$d = -27/r_l^{1.65},$$

$$e = -58/r_l^{1.9},$$

$$f = (15/r_l)^4 + 1.13,$$

$$g = (16.7/r_l)^8 + 0.004r_l + 1,$$

with the radii expressed in micrometers.

Berry and Pranger (1974) have developed an empirical expression for the terminal velocity of the form

$$v(D) = \frac{\eta \text{Re}}{D\rho}, \quad \text{(B2.9)}$$

where Re is the Reynolds number for the airflow around the drops, and where η, the dynamic viscosity of the air, is given by the relation

$$\eta = 1.496286\ 10^{-6}\frac{T^{1.5}}{T + 120}. \quad \text{(B2.10)}$$

The following expressions for Reynolds number have been obtained from the data for Beard and Pruppacher (1969) and Gunn and Kinzer (1949):

$$\text{Re} = 0.0412657y - 1.50074\ 10^{-4}y^2 + 7.58884\ 10^{-7}y^3 - 1.68841\ 10^{-9}y^4$$

when $0 < y \leq 175.27$, and by

$$\text{Re} = \exp[-2.36534 + 0.767787\ \ln y + 0.00535826(\ln y)^2 - 7.63554\ 10^{-4}(\ln y)^3]$$

when $175.27 < y \leq 10^7$. The parameter y is given by

$$y = \frac{4\rho\rho_l g}{3\eta^2} D^3.$$

B3. Selfcollection

Selfcollection is the process by which collisions between raindrops produce larger drops. In contrast to the previous discussion of growth by accretion, the interacting drops are of the same size range. It is therefore necessary to envisage here (as for autoconversion) a stochastic coalescence mode.

Let $n(V)$ be the number of drops per unit volume of air. If selfcollection is the only process considered, the variation of $n(V)$ can be represented by the following equation:

$$\left.\frac{\partial(n(V))}{\partial t}\right|_{\text{self}} = \frac{1}{2}\int_{\hat{V}}^{V-V'} n(V-V')n(V')K(V-V', V') \times dV' - \int_{\hat{V}}^{\infty} n(V)n(V')K(V, V')dV', \quad \text{(B3.1)}$$

where $\hat{V}$ is the volume of the smallest drops (the drops smaller than this size belong to the category of cloud droplets), and where $K(V, V') = K(D, D')$ is the collection kernel of a drop of diameter D' (volume V') by a drop of diameter D (volume V).

The first integral on the right side of (B3.1) is a source term: two drops of volume greater than $\hat{V}$ but less than V collide to form a drop of volume V. The second integral constitutes a sink term: a drop of volume V encounters another raindrop, and its volume becomes larger than V.

Upon integrating over the entire spectrum, we obtain:

$$\left.\frac{\partial N_r}{\partial t}\right|_{\text{self}} = \frac{1}{2}\int_{2\hat{V}}^{\infty}\int_{\hat{V}}^{V-V'} n(V-V')n(V')K(V-V', V') \times dV'dV - \int_{\hat{V}}^{\infty}\int_{\hat{V}}^{\infty} n(V)n(V')K(V, V')dV'dV. \quad \text{(B3.2)}$$

Let us denote the first double integral as $I1$ and the second as $I2$. To evaluate $I1$, we first permute the order of integration. After making the change of variable $V'' = V - V'$,

$$I1 = \int_{\hat{V}}^{\infty}\int_{\hat{V}}^{\infty} n(V'')n(V')K(V'', V')dV''dV', \quad \text{(B3.3)}$$

and $I1 = I2$. Equation (B3.2) then becomes

$$\left.\frac{\partial N_r}{\partial t}\right|_{\text{self}} = -\frac{1}{2}\int_{\hat{V}}^{\infty} n(V)\int_{\hat{V}}^{\infty} n(V')K(V, V')dV'dV. \quad \text{(B3.4)}$$

Upon expressing (B3.4) in terms of diameter, and making the substitution

$$b_s(D, D') = \frac{K(D, D')}{m(D) + m(D')} = \frac{3D^2}{2\rho_l(D^3 + D'^3)}\gamma_c^2(D, D')[v(D) - v(D')], \quad \text{(B3.5)}$$

we obtain

$$\left.\frac{\partial N_r}{\partial t}\right|_{\text{self}} = -\frac{1}{2}\int_{\hat{D}}^{\infty}\int_{\hat{D}}^{\infty} n(D)n(D')m(D)b_s(D, D')dD'dD - \frac{1}{2}\int_{\hat{D}}^{\infty}\int_{\hat{D}}^{\infty} n(D)n(D')m(D')b_s(D, D')dD'dD. \quad \text{(B3.6)}$$

After permuting the order of integration in the second integral, we obtain

$$\left.\frac{\partial N_r}{\partial t}\right|_{\text{self}} = -\int_{\hat{D}}^{\infty} m(D)n(D)\int_{\hat{D}}^{\infty} n(D')b_s(D, D')dD'dD. \quad \text{(B3.7)}$$

Using the same calculation procedure as in the previous discussion of accretional growth, (Section B3) we know that there exist D^* and $\tilde{D}$ such that

$$\left.\frac{\partial N_r}{\partial t}\right|_{\text{self}} = -b_s(\tilde{D}, D^*)N_r\rho q_r. \quad \text{(B3.8)}$$

In the parameterizations of Berry and Reinhardt, $\tilde{D} = D_{gr}$ and $D^* = \overline{D_r}$, with the same notation as before.

B4. Sedimentation

The flux of raindrop concentration through a unit horizontal surface may be written

$$F_N = \int_0^{\infty} n(D)[v(D) - w]dD = \int_0^{\infty} n(D)v(D)dD - wN_r. \quad \text{(B4.1)}$$

With the same notation as before, we use (B2.9) for the terminal fall velocity expressed in terms of Reynolds number and dynamic viscosity. Berry and Pranger (1974) give the following expression for the Reynolds number:

$$R_e(D) = \exp[c_1 + c_2(\ln y) + c_3(\ln y)^2], \quad \text{(B4.2)}$$

where

$$c_1 = -3.12611,$$
$$c_2 = 1.01338,$$
$$c_3 = -0.0191182,$$

and where

$$y = \left(\frac{4\rho\rho_l g}{3\eta^2}\right)D^3 = aD^3.$$

If we let X denote the dimensionless ratio D/D_0, then we may express S_N, the sedimentation term in (B4.1), as

$$S_N = \int^{\infty} n(D)v(D)dD$$
$$= \int^{\infty} n(D_0X)v(D_0X)D_0dX. \quad \text{(B4.3)}$$

Now

$$\mathrm{Re}(D) = \mathrm{Re}(D_0X) = k_1X^{k_2}\exp(9c_3\ln^2X), \quad \text{(B4.4)}$$

where

$$k_1 = \exp[c_1 + c_2\ln(aD_0^3) + c_3\ln^2(aD_0^3)] = \mathrm{Re}(D_0),$$

$$k_2 = 3c_2 + 6c_3\ln(aD_0^3).$$

We then have

$$v(D_0X) = \frac{\eta k_0X^{k_2-1}}{D_0\rho}\exp(9c_3\ln^2X),$$

$$n(D_0X) = \frac{N_r}{(2\pi)^{1/2}\sigma_0D_0X}\exp\left(-\frac{1}{2\sigma_0^2}\ln^2X\right).$$

The sedimentation term (B4.3) then becomes

$$S_n = \frac{N_r\eta k_1}{(2\pi)^{1/2}\sigma_0\rho D_0}\int_0^{\infty} X^{k_2-1} \times \exp\left[-\left(\frac{1}{2\sigma_0^2} - 9c_3\right)\ln^2X\right]\frac{dX}{X}. \quad \text{(B4.5)}$$

Since $(\frac{1}{2}\sigma_0^2 - 9c_3)$ is always positive, we define $p^2 = (\frac{1}{2}\sigma_0^2 - 9c_3)$ and evaluate the integral to obtain the result

$$S_n = \frac{N_rv(D_0)}{(2\pi)^{1/2}\sigma_0p}\exp\left[\frac{(k_2-1)^2}{4p^2}\right]. \quad \text{(B4.6)}$$

We now let S_q be the sedimentation term for the rainwater mixing ratio.

$$S_q = \int_0^{\infty}\frac{m(D)}{\rho}n(D)v(D)dD$$
$$= \frac{\pi\rho_lD_0^3}{6\rho}\int_0^{\infty}X^3n(D_0X)v(D_0X)D_0dD. \quad \text{(B4.7)}$$

After integration, one then obtains an equivalent expression for S_q:

$$S_q = \frac{q_0v(D_0)}{(2\pi)^{1/2}\sigma_0p}\exp\left[\frac{(k_2+2)^2}{4p^2}\right], \quad \text{(B4.8)}$$

where

$$q_0 = \frac{N_rm(D_0)}{\rho}.$$

Finally, the sedimentation terms in (12) and (13) are written

$$\left.\frac{\partial N_r}{\partial t}\right|_{\mathrm{sed}} = \frac{\partial S_n}{\partial z} \quad \text{(B4.9)}$$

$$\left.\frac{\partial q_r}{\partial t}\right|_{\mathrm{sed}} = \frac{\partial S_q}{\partial z}. \quad \text{(B4.10)}$$

B5. Rain evaporation

The evaporation of a raindrop of diameter D is given by $dD/dt = AS\bar{f}/D$, where A is a thermodynamical function of pressure and temperature, S is the undersaturation, and $\bar{f}$ is a ventilation coefficient.

Pruppacher and Rasmussen (1979) give a parameterization for $\bar{f}$ as a function of Reynolds and Schmidt numbers which leads to the following fit as a function of diameter

$$\bar{f} = -4.33\ 10^5D^2 + 5.31\ 10^3D + 0.572. \quad \text{(B5.1)}$$

The integration of (B5.1) over the whole spectrum gives for the evaporation term

$$\left.\frac{\partial q_{rw}}{\partial t}\right|_{\mathrm{eva}} = \frac{\rho_l}{\rho}\frac{\pi}{2}ASN_r\left[0.572D_0\exp\left(\frac{\sigma_r^2}{2}\right) + 5.31\ 10^3D_0^2\exp(2\sigma_r^2) - 4.33\ 10^5D_0^3\exp\left(\frac{9\sigma_r^2}{2}\right)\right]. \quad \text{(B5.2)}$$

The number of raindrops which completely evaporate during one model time step is given by

$$N_{r_{\mathrm{eva}}} = \frac{1}{\Delta t}\int_0^{D_{\mathrm{crit}}}\frac{N_r}{(2\pi)^{1/2}\sigma D}\exp\left(-\frac{1}{2\sigma^2}\ln^2\frac{D}{D_0}\right)dD, \quad \text{(B5.3)}$$

where D_{crit} is found by equating

$$\int_{D_{\mathrm{crit}}}^0 DdD = \int_t^{t+\Delta t} ASdt.$$

Here it is assumed that the drops which completely evaporate during one time step are small enough that the ventilation effect can be ignored.

Assuming AS to be constant over one time step, we then obtain $D_{\mathrm{crit}} = (-2AS\Delta t)^{1/2}$ (where S is negative). $N_{r_{\mathrm{eva}}}$ is removed from N_r after the prediction.

REFERENCES

Alaka, M. A. (Ed.), 1960: The airflow over mountains. WMO Tech. Note 34, 135 pp.

Anthes, R. A., and T. T. Warner, 1978: The development of mesoscale models suitable for air pollution and other mesometeorological studies. *Mon. Wea. Rev.*, **106**, 1045–1078.

——, and P. L. Haagenson, 1983: A comparative numerical simulation of the Sichuan flooding catastrophe (11–15 July 1981). *Proc. First Sino-American Workshop on Mountain Meteorology*, Beijing, Amer. Meteor. Soc., 519–524.

Beard, K. V., and H. R. Pruppacher, 1969: A determination of the

terminal velocity and drag of small water drops by means of a wind tunnel. *J. Atmos. Sci.*, **26,** 1066–1072.

Benoit, R., 1977: On the integral of the surface layer profile-gradient functions. *J. Appl. Meteor.*, **16,** 859–860.

Bergeron, T., 1965: On the low-level redistribution of atmospheric water caused by orography. *Suppl. Proc. Int. Conf. on Cloud Physics,* Tokyo, 96–100.

Berry, E. X., 1967: Cloud droplet growth by collection. *J. Atmos. Sci.*, **24,** 688–701.

——, and R. L. Reinhardt, 1973: Modeling of condensation and collection within clouds. D.R.I. Phys. Sci. Pub. No. 16, University of Nevada.

——, and M. P. Pranger, 1974: Equations for calculating the terminal velocities of water drops. *J. Appl. Meteor.*, **13,** 108–113.

Browning, K. A., F. F. Hill and C. W. Pardoe, 1974: Structure and mechanism of precipitation and the effect of orography in a wintertime warm sector. *Quart. J. Roy. Meteor. Soc.*, **100,** 309–330.

Chang, C. B., D. J. Perkey and C. W. Kreitzberg, 1981: A numerical study of the squall line of 6 May 1975. *J. Atmos. Sci.*, **38,** 1601–1615.

Clark, T. L., 1979: Numerical simulations with a three-dimensional cloud model: Lateral boundary condition experiments and multicellular severe storm simulations. *J. Atmos. Sci.*, **36,** 2191–2215.

De Rivas, E. K., 1972: On the use of nonuniform grids in finite difference equations. *J. Comput. Phys.*, **10,** 202–210.

Dufour, L., and J. Van Mieghem, 1975: Thermodynamique de l'atmosphere. Institut Royal Meteorologique de Belgique, Brussels.

Durran, D. R., and J. B. Klemp, 1983: A compressible model for the simulation of moist mountain waves. *Mon. Wea. Rev.*, **111,** 2341–2361.

Gunn, R., and G. D. Kinzer, 1949: The terminal velocity of fall for water droplets in stagnant air. *J. Meteor.*, **6,** 243–248.

Hess, S. L., 1959: *Introduction to Theoretical Meteorology,* Holt-Dryden, 362 pp.

Klemp, J. B., and D. K. Lilly, 1978: Numerical simulation of hydrostatic waves. *J. Atmos. Sci.*, **35,** 78–107.

Lavoie, R. L., et al., 1967: The warm rain project in Hawaii. *Tellus,* **19,** 347–461.

Mahrer, Y., and R. A. Pielke, 1978: A test of an upstream spline interpolation technique for the advective terms in a numerical mesoscale model. *Mon. Wea. Rev.*, **106,** 818–830.

Markowitz, A. H., 1976: Raindrop size distribution expressions. *J. Appl. Meteor.*, **15,** 1029–1031.

Nickerson, E. C., 1979: On the numerical simulation of airflow and clouds over mountainous terrain. *Beitr. Phys. Atmos.*, **52,** 161–177.

——, and V. E. Smiley, 1975: Surface layer and energy budget parameterization for mesoscale models. *J. Appl. Meteor.*, **14,** 297–300.

O'Brien, J., 1970: On the vertical structure of the eddy exchange coefficient in the planetary boundary layer. *J. Atmos. Sci.*, **27,** 1213–1215.

Orlanski, I., 1976: A simple boundary condition for unbounded hyperbolic flows. *J. Comput. Phys.*, **21,** 251–269.

Pielke, R. A., 1981: Mesoscale numerical modeling. *Advances in Geophysics,* **23,** Academic Press, 185–344.

Pruppacher, H. R., and R. Rasmussen, 1979: A wind tunnel investigation of the rate of evaporation of large water drops falling at terminal velocity in air. *J. Atmos. Sci.*, **36,** 1255–1260.

Salinger, M. J., 1980: New Zealand Climate: I. Precipitation patterns. *Mon. Wea Rev.*, **108,** 1892–1904.

Schlesinger, R. E., L. W. Uccellini and D. R. Johnson, 1983: The effects of the Asselin time filter on numerical solutions to the linearized shallow-water wave equations. *Mon. Wea. Rev.*, **111,** 455–467.

Shafrir, U., and M. Neiburger, 1963: Collision efficiencies of two spheres falling in a viscous medium. *J. Geophys. Res.*, **68,** 4141–4148.

Shapiro, R., 1970: Smoothing, filtering and boundary effects. *Rev. Geophys. Space Phys.*, **8,** 359–387.

Smith, R. B., 1979: The influence of mountains on the atmosphere. *Advances in Geophysics,* **21,** Academic Press, 87–230.

Stearns, L. P., 1983: Infrared cooling in cloudy atmospheres: Precision of grid point selection for numerical models. *Mon. Wea. Rev.*, **111,** 1501–1505.

Sutton, O. G., 1953: *Micrometeorology.* McGraw-Hill, New York.

Takahashi, T., 1979: Warm cloud electricity in a shallow axisymmetric cloud model. *J. Atmos. Sci.*, **36,** 2236–2258.

Tarbell, T. C., T. T. Warner and R. A. Anthes, 1981: An example of the initialization of the divergent wind component in a mesoscale numerical prediction model. *Mon. Wea. Rev.*, **109,** 77–95.

Young, K. C., 1974: A numerical simulation of wintertime orographic precipitation: Part I. Description of model microphysics and numerical techniques. *J. Atmos. Sci.*, **31,** 1735–1748.

Warner, T. T., R. A. Anthes and A. L. McNab, 1978: Numerical simulations with a three-dimensional mesoscale model. *Mon. Wea. Rev.*, **106,** 1079–1099.

Weickmann, H. K., 1979: Tor Harold Percival Bergeron. *Bull. Amer. Meteor. Soc.*, **60,** 406–414.